Bioactive Materials 6 (2021) 262–272

Contents lists available at ScienceDirect

Bioactive Materials

journal homepage: http://www.keaipublishing.com/biomat

Nano-micrometer surface roughness gradients reveal topographical influences on differentiating responses of vascular cells on biodegradable magnesium

Ke Zhou[a,1], Yutong Li[a,1], Lei Zhang[a], Liang Jin[a], Feng Yuan[b], Jinyun Tan[c,***], Guangyin Yuan[a,**], Jia Pei[a,*]

[a] National Engineering Research Center of Light Alloy Net Forming & State Key Laboratory of Metal Matrix Composite, School of Materials Science & Engineering, Shanghai Jiao Tong University, 800 Dongchuan Road, Shanghai, 200240, China
[b] Department of Biomedical Engineering, University of Texas at Austin, TX, 78712, USA
[c] Department of Vascular Surgery, Huashan Hospital, Fudan University, Shanghai, 200040, China

ARTICLE INFO

Keywords:
Surface roughness gradients
Topography cue
Vascular cells
Cell adhesion and proliferation
Cell selectivity

ABSTRACT

Distinctively directing endothelial cells (ECs) and smooth muscle cells (SMCs), potentially by surface topography cue, is of central importance for enhancing bioefficacy of vascular implants. For the first time, surface gradients with a broad range of nano-micrometer roughness are developed on Mg, a promising next-generation biodegradable metal, to carry out a systematic study on the response of ECs and SMCs. Cell adhesion, spreading, and proliferation are quantified along gradients by high-throughput imaging, illustrating drastic divergence between ECs and SMCs, especially in highly rough regions. The profound role of surface topography overcoming the biochemical cue of released Mg^{2+} is unraveled at different roughness ranges for ECs and SMCs. Further insights into the underlying regulatory mechanism are gained at subcellular and gene levels. Our work enables high-efficient exploration of optimized surface morphology for modulating favored cell selectivity of promoting ECs and suppressing SMCs, providing a potential strategy to achieve rapid endothelialization for Mg.

1. Introduction

Cardiovascular disease has been a dominant threat to human health and death globally for decades [1]. Stent implantation and vascular grafts serve as the primary treatments of the fatal disease. Since the first case of percutaneous transluminal coronary angioplasty in 1977 [2], the percutaneous coronary intervention has experienced a cascade of development from simple balloon dilation, bare metal stent (BMS), to drug-eluting stent (DES) [3]. However, accumulative clinical evidence indicates the occurrence of adverse problems, in particular, post-operative in-stent restenosis (ISR), leading to a relatively high re-intervention rate. Previous reports have demonstrated that ISR is predominately caused by the excessive proliferation of smooth muscle cells (SMCs) and neointima hyperplasia [4]. While the DES approach inhibits SMCs and consequently diminishes ISR to some extent via releasing anti-proliferation drugs [5,6], it could also indiscriminately impair the viability and growth of endothelial cells (ECs) and thus delaying re-endothelialization post stenting. Such suppression effect on ECs is undesirable, as ECs play an essential role in regulating coronary function, controlling SMCs migration and proliferation, and preventing platelet activation. Furthermore, re-endothelialization promotes the healing of the arterial wall and facilitates the maintaining of vascular integrity and functions [7]. On the contrary, inadequate re-endothelialization is reported to be closely correlated to the increased rate of late restenosis and thrombosis [8]. Therefore, fostering rapid re-endothelialization, meanwhile impeding SMCs proliferation, is essential in determining the clinical outcomes.

In addition to (bio)chemical cues such as growth factors and cytokines [9], increasing reports suggest that cells respond to physical cues as well, especially surface topography at the subcellular scale of

Peer review under responsibility of KeAi Communications Co., Ltd.

* Corresponding author.
** Corresponding author.
*** Corresponding author.
E-mail addresses: m.tan@fudan.edu.cn (J. Tan), gyyuan@sjtu.edu.cn (G. Yuan), jpei@sjtu.edu.cn (J. Pei).

[1] These authors contributed equally to this work and should be considered co-first authors.

https://doi.org/10.1016/j.bioactmat.2020.08.004
Received 4 July 2020; Received in revised form 5 August 2020; Accepted 8 August 2020

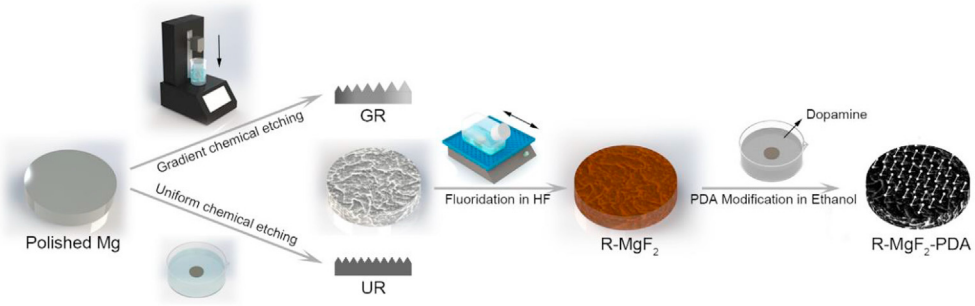

Fig. 1. Illustration of the preparation process of coated Mg samples with defined surface roughness.

micrometer and nanometer range [10], which in turn display alterations in proliferation, adhesion, differentiation, apoptosis, and other functions in a directed manner, namely contact guidance [11]. Cellular responses are intensively specific to topographic parameters of shape, size, and arrangement, as well as cell type. In the last decade, extensive efforts have been made to study the interactions of ECs, SMCs, or both with varying topography stimuli, with some reported to achieve selective modulation of the vascular cells. Among them, the influence of various surface morphology profiles including regular grooves [12], pillars [13], and pits [14], and irregular morphology of defined roughness parameters have been investigated [15], where substrates of polymers (PDMS, PVC, PS and PLA), ceramics (silicon, bulk metallic glass) and metals (Al_2O_3, TiO_2, stainless steel and CoCr) were employed. For example, Ding et al. reported 1 μm groove pattern on silicon wafers coated with a thin layer of titanium oxide was able to improve the ECs attachment and proliferation *in vitro* [14]. Similar surface morphology was prepared by Liang et al. on 316L cardiovascular stent and indicated enhanced re-endothelialization post-implantation into the iliac artery of rabbits [16]. Nevertheless, some of the findings appeared contradictory or remained controversial due to the intervention of different surface chemistry or other factors. Besides, a large portion of the utilized substrates had little relevance to the vascular implant materials in clinical use. To date, systematic investigation of adhesion and proliferation of both ECs and SMCs in response to defined surface roughness in the entire nano to micro range on implant-relevant substrates has rarely been reported, and thus requires in-depth elucidation.

In order to comprehensively probe the cell behaviors in response to various surface cues, surface gradients with physical or chemical properties that gradually change over a given distance on samples can provide an efficient and high-throughput platform. The deployment of gradients allows for exploring the effect of continuously varying surface parameters within a single experiment [17], with minimized system errors and saved cost. Previous reports have demonstrated the feasibility and advantages of the surface gradient approach in the study of the response of a variety of cells, including endothelial colony-forming cells [13], MC3T3-E1 osteoblastic cells [18], and human mesenchymal stem cells [19]. While methods to fabricate morphological gradients mainly include particle binding, electrochemical etching, erosion/chemical polishing—replica [17], the substrates used are often limited to silicon or glass with entirely different characteristics from biodegradable materials. Meanwhile, most of these approachs could not simultaneously cover a broad nano-micrometer range. Moreover, properties such as corrosion resistance and cytocompatibility should also be taken into consideration when constructing topological gradients to study interfacial cell interactions, which poses considerable restrictions on suitable fabrication methodology.

Magnesium and magnesium alloys, as a promising candidate for the new-generation biodegradable material [20,21], are capable of mitigating chronic inflammation caused by the long-term retention of non-degradable materials (i.e., NiTi and CoCr alloys) in the human body. Moreover, the main degradation products, Mg^{2+}, one of the most abundant intracellular cations, is known to play a regulatory role in the viability, proliferation, and functions of ECs and SMCs [22]. To date, how vascular cells respond to topography cues in the presence of biochemical cue of Mg^{2+} remains unresolved. Herein, a Mg-Nd-Zn-Zr alloy (denoted as Mg) previously developed with desirable mechanical properties, acceptable biocompatibility, and uniform degradation characteristics, was used as the substrate [23]. A facile and reproducible method of dip-etching into citric acid was implemented to obtain surface roughness gradients (denoted as GR) on Mg, where the uniformly distributed, nanophasic second phase was employed as the template to generate ridge/valley features [24]. Moreover, this approach is also compatible with the subsequent surface modification. The as-prepared gradients provided a broad roughness range of Sa between 0.1 and 2.0 μm, following the anti-corrosion treatment of MgF_2/Polydopamine (PDA) coating to maintain mild Mg degradation and enhance cytocompatibility [25], as shown in Fig. 1. The behaviors of vascular ECs and SMCs, including adhesion, spreading, and proliferation, could be directly microscopically observed along the obtained roughness gradients. Uniform roughness samples (denoted as UR) were used for examination of sample degradation and for further confirmation of obtained cellular results on gradients.

2. Material and methods

2.1. Preparation of coated gradient samples

Mg-Nd-Zn-Zr alloy previously developed was used as the substrate Mg alloy material, of which the chemical composition and the processing could be found in the report [26]. Mg disk samples were cut from the extruded rod to the size of Φ20 mm × 3 mm for gradient samples preparation, and Φ14 mm × 3 mm for uniform roughness samples. Afterward, samples were ground progressively with SiC grinding paper up to 7000 #, followed by further polishing with magnesium oxide powder slurry. Polished Mg substrates were consecutively ultrasonically cleaned in acetone and ethanol for 10 min and dried with a stream of air.

The preparation process of coated Mg roughness samples was conducted as follows. Firstly, surface roughness feature was generated. For the roughness gradient samples (GR), Mg substrates were gradually dipped into 0.25 mol/L citric acid solution (Sinopharm Group Co., Ltd., Shanghai) controlled by a programmed dip-coater (SYDC-100, Shanghai Yanyan Materials Technology Co., Ltd, China) at room temperature. By the end of the dipping process, samples were immediately removed and rinsed with a copious amount of DI water. Following that, samples were ultrasonically cleaned in ethanol for 3 min and dried with a stream of air. Meanwhile, uniform roughness samples (UR) were fabricated according to the corresponding etching time in citric acid.

The rough samples were subsequently subjected to a thin coating to enhance anti-corrosion ability and biocompatibility. Briefly, the etched samples were treated with 40 wt% hydrofluoric acid (Sinopharm Group Co., Ltd., Shanghai) for 12 h to form a dense conversion layer of MgF_2

(GR-MgF_2). Subsequently, samples were dipped into 1 mg/ml of dopamine hydrochloride solution (95% vol. ethanol, Alfa Aesar, USA) for 24 h, where a slight amount of $NH_3{\cdot}H_2O$ (25–28 wt%, Sinopharm Group Co., Ltd., Shanghai) was added to trigger DA polymerization and PDA deposition. Finally, the coated roughness gradient samples (GR-MgF_2-PDA) were ultrasonically cleaned in ethanol and DI water for 1 min, respectively, and dried with a stream of nitrogen.

2.2. Surface characterizations of gradient samples

Surface roughness and morphology of the as-prepared GR-MgF_2-PDA samples were measured with an Optical Surface Metrology System (Leica DCM8, Leica, Germany) in confocal mode. The arithmetical mean deviation of the surface (Sa) was calculated using Leica Map software with measurements of at least five points on each position along a gradient sample and at least three samples for a batch.

Surface microstructure and element composition of gradient samples were evaluated by scanning electron microscopy coupled with energy-dispersive X-ray spectroscopy (SEM-EDS, Mira3 & Aztec X-MaxN80, TESCAN, Czech Republic). Prior to SEM observation, samples were coated with a thin layer of gold by a sputter coater (SHINKKU VD MSP-IS, Japan).

To obtain surface chemical information upon surface modification, UR samples, and UR-MgF_2-PDA samples were subjected to microscopes Fourier-transform infrared spectroscopy (FT-IR) measurement using a Nicolet iN 10 MX spectroscopy (Thermo Fisher Scientific, USA). Scans were performed from 675 to 4000 cm^{-1}, and data were analyzed by OMNIC software (Version 8.2, Thermo Fisher Scientific, USA).

Static contact angle measurements along the gradient samples were performed by a contact angle instrument (JC2000D1, Powereach, China), utilizing the sessile drop method. The mean value was obtained from at least three individual measurements at different positions along each gradient sample.

2.3. In vitro degradation

Uniform samples of varying roughness (UR-MgF_2-PDA) were immersed in cell culture medium (DMEM, Gibco, USA) and placed in a cell incubator at 37 °C with 5% CO_2 to obtain the supernatants (sample extracts) at 1 day, 3 days and 5 days. The ratio of the sample area to solution volume was set as 1.25 cm^2/mL, according to ISO 10993–5. The concentrations of Mg^{2+} in the sample extracts at 1 day, 3 days, and 5 days were analyzed with an inductively coupled plasma atomic emission spectrometer (ICP-AES, iCAP6300, USA). The pH and osmotic pressure were measured with a pH meter (B711, Horiba, Japan), and freezing point osmometer (Osmomat 3000, Gonotec, Germany), respectively.

2.4. Cell culture

ECs (EA.hy926 cell line) and SMCs (A7r5 cell line) (Cell Bank, Chinese Academy of Sciences) were respectively cultured in 10% fetal bovine serum (FBS, Gibco, USA) and 1% Penicillin & Streptomycin (PS, Hyclon, USA) DMEM medium and placed in a cell incubator at 37 °C in a humidified atmosphere with 5% CO_2. The culture medium was refreshed every 2 days. After reaching ~80% confluence, cells were subcultured using 0.25% trypsin-EDTA (Gibco, USA). Cells of passage 3rd-7th were used for the experiments. The cell seeding density for the experiments was determined utilizing the Automated Cell Counter (IC1000, Countstar, China).

2.5. Cell viability assay

The extracts of UR-MgF_2-PDA samples were prepared as previously described in the **2.3** section. Cells were seeded in 96-well plates at a density of 1×10^4 cells/mL with 100 μL of DMEM medium for each well and allowed for attachment for 24 h. Subsequently, the medium was replaced with the sample extracts supplemented with 10% FBS. After cultured for 1 day and 3 days, respectively, 10 μL of CCK-8 kit solution (Beyotime Biotechnology, China) was added into each well and incubated for 2 h in a cell incubator. Finally, the optical density (OD) value of each well was measured at 450 nm wavelength with a microplate reader (iMARK, Bio-Rad, USA). Cell viability was calculated according to **Equation (1)**.

$$\text{Cell viability}\ (\%) = \frac{OD_{samples} - OD_{blank}}{OD_{negative\ control} - OD_{blank}} \times 100\% \quad (1)$$

2.6. Direct cell adhesion and proliferation assay on gradient samples

Cells were seeded onto GR-MgF_2-PDA samples in 12-well plates at a density of 1×10^4 cells/mL and cultured for 6 h, 1 d, and 3 d. Afterward, samples were gently rinsed twice with PBS solution (Dulbecco's Phosphate Buffered Saline) pre-warmed to 37 °C, followed by fixation in 4 wt% paraformaldehyde solution (PFA, Sigma-Aldrich, USA) for 20 min. After rinsing with PBS, the adherent cells were permeabilized with 0.5% TritonX-100 for 5 min. Subsequently, samples were incubated overnight with primary anti-vinculin antibody (V9131, Sigma-Aldrich, USA) in 1% BSA/PBS solution, followed by incubation with secondary goat anti-mouse antibody labeled with Alexa 594 (1:300 dilution in PBS, Invitrogen, USA) for 1 h and then rinsed with PBS. Cells were subsequently stained with Alexa Fluor 488 phalloidin (1:100 dilution in PBS, Invitrogen, USA) for 30 min and rinsed twice with PBS. Cell nuclei were then stained with DAPI (1:1000 dilution in PBS, Invitrogen, USA) for 10 min, followed by a gentle rinse with PBS. Finally, samples were mounted and subjected to fluorescence microscopy observation (IX71, Olympus, Japan). At least four images were taken at each position along the gradient samples. The adherent cell number and cell spreading area were analyzed with ImageJ software (Java 1.8.0_112, NIH, USA).

For SEM observation of cell morphology and attachment, PFA-fixed samples were dehydrated with graded concentrations of ethanol (30%, 50%, 70%, 90%, and 100%) for 15min each. Afterward, samples were treated with critical point drying (Autosamdri-931, Tousimis, USA) in auto-mode, then coated with a thin film of Au for conductivity and finally observed with SEM.

2.7. Cell adhesion assay in simulated Mg degradation microenvironment

Cells were seeded in 6-well transwell plates at a density of 1.25×10^4 cells/mL in DMEM and allowed for attachment for 1 h. Subsequently, a rough sample with coating was placed on the upper compartment of transwell, immersed with culture medium to generate a simulated Mg degradation microenvironment, while cells seeded on the bottom plate could then be studied for adhesion and proliferation. Cells cultured without Mg samples in DMEM were employed as blank control. After incubated for 6 h, 1 day, and 3 days, the culture medium was collected to analyze released Mg^{2+} concentrations with ICP-AES. Meanwhile, the adherent cells on the bottom of the transwell plate were PFA-fixed, stained, and subjected to fluorescence microscopy according to the **2.6** section.

2.8. Real-time quantitative PCR (RT-qPCR) analysis

Cells were seeded on the uniform specimens (UR-MgF_2-PDA) of varying roughness at a density of 1.25×10^5 cells/mL for 24 h. Total RNA was collected using Trizol reagent (Invitrogen, USA) according to the manufacturer's instruction. The concentration and purity of total RNA were examined by Nanodrop 2000 (Thermo Fisher Scientific, USA). Subsequently, the cDNA synthesis was carried out according to the protocol (TOYOBO, Japan). Finally, Bio-Rad C1000 was used for

RT-qPCR analysis with SYBR® Green Real-time PCR Master Mix (TOYOBO, Japan). The expressions of proliferating cell nuclear antigen (PCNA) and vinculin (VCL) were analyzed for both ECs and SMCs. For ECs, endothelial nitric oxide synthase (eNOs) was also measured. Glyceraldehyde 3-phosphate dehydrogenase (GAPDH) was employed as the reference gene for ECs, and β-actin was utilized for SMCs. The expression level of the genes was evaluated using the $2^{-\Delta\Delta Ct}$ method and normalized to the reference genes. The primers used for RT-qPCR are shown in Table S1.

2.9. Statistical analysis

The results are expressed as the mean ± standard deviation of each sample. All cellular experiments were independently repeated for at least three times. The results were analyzed with Student's *t*-test or one-way analysis of variance (ANOVA) using SPSS software (Version 24, IBM, USA). *, ** and *** indicate the level of significance $P < 0.05$, 0.01 and 0.001, respectively.

3. Results

3.1. Surface physicochemical characterizations

A representative photograph of the surface roughness gradients obtained through acid etching on Mg samples is shown in Fig. 2a, revealing a macroscopic surface change in one dimension, from smooth polished state to increasingly coarse morphology along the sample. The 3D surface metrology images of six different positions along the roughness gradient samples (GR) are displayed in Fig. 2b. The Gaussian distribution of surface height indicated the evolution of networks comprised of ridge/valley-like structures on Mg samples, with increasing feature density and height difference along the etched gradient samples. In Fig. 2c, the statistical results of surface roughness demonstrated a linear relationship ($R^2 = 0.987$) between the Sa values and the distance along the GR-MgF_2-PDA samples, which verified a gradual rise of surface roughness Sa between 0.12 and 2.0 μm, along with the variation of Rz between 0.34 and 6.3 μm. Notably, subsequent surface modifications of fluorination and PDA ultrathin coating barely caused obvious alteration of the Sa values along the etched GR samples (Fig. S1).

Further characterization with SEM (Fig. 3a) confirmed the etched ridge/valley-like patterns, gradually forming interconnected networks as the Sa increased. Note that the large number of whitish, nano-scale particles randomly distributed at Sa of 0.1 μm correspond to the second phase $Mg_{12}Nd$ [24]. To further analyze the topography formation mechanism, surface element composition post etching was measured. EDS results (Table S2) of high-magnification SEM (Fig. 3b and c) suggested the composition of the ridges was quite close to that of $Mg_{12}Nd$, while the basic phase predominated the valley regions. As the second phase was reported of a slightly higher electrode potential by ~25 mV [23], Mg basic phase was preferentially attacked and eventually formed the etched pits. It suggested the nano-phasic second phase served as the template for acid etching to generate the structures on Mg.

To examine the subsequent anti-corrosion modification, Fig. 3d and

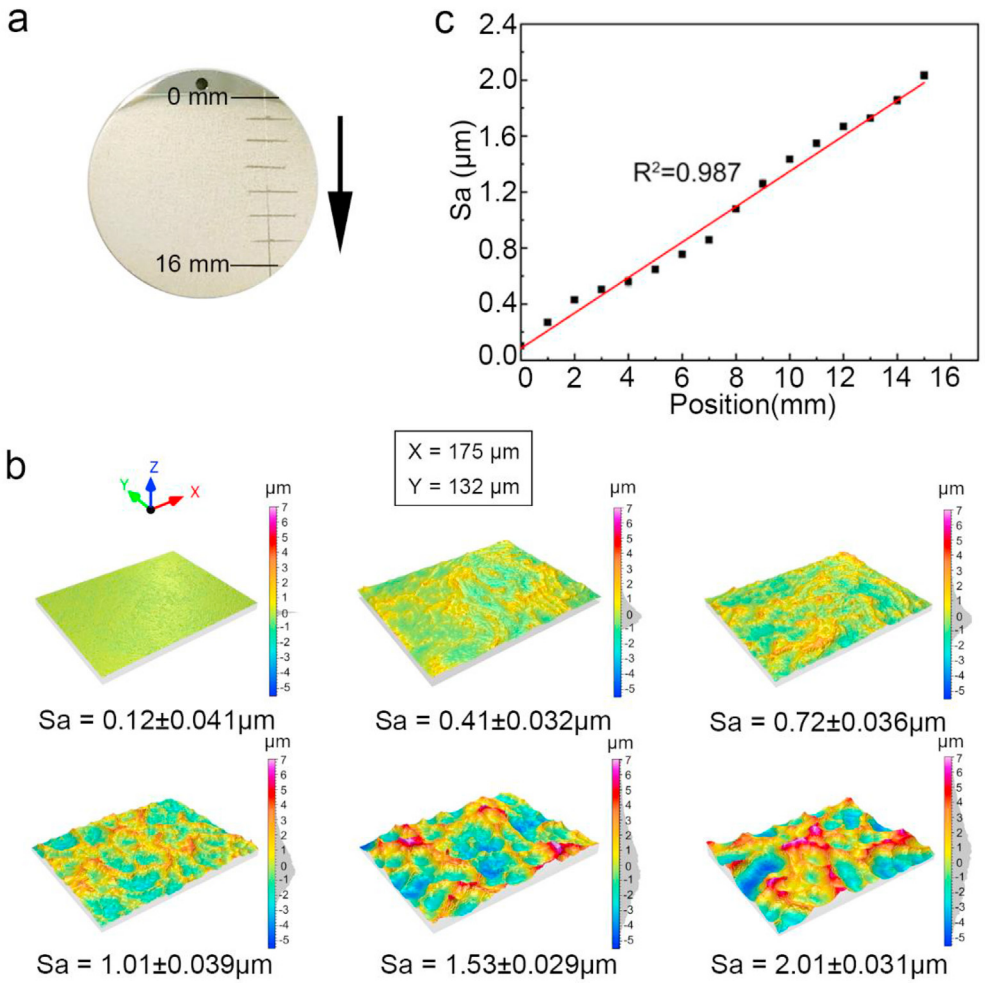

Fig. 2. (a) Photograph of an etched gradient sample, (b) 3D surface metrology images of six positions (corresponding to Sa = 0.1, 0.4, 0.7, 1.0, 1.5, and 2.0 μm) along a gradient, and (c) statistical results of Sa values as a function of the distances along the gradients (statistical error presented).

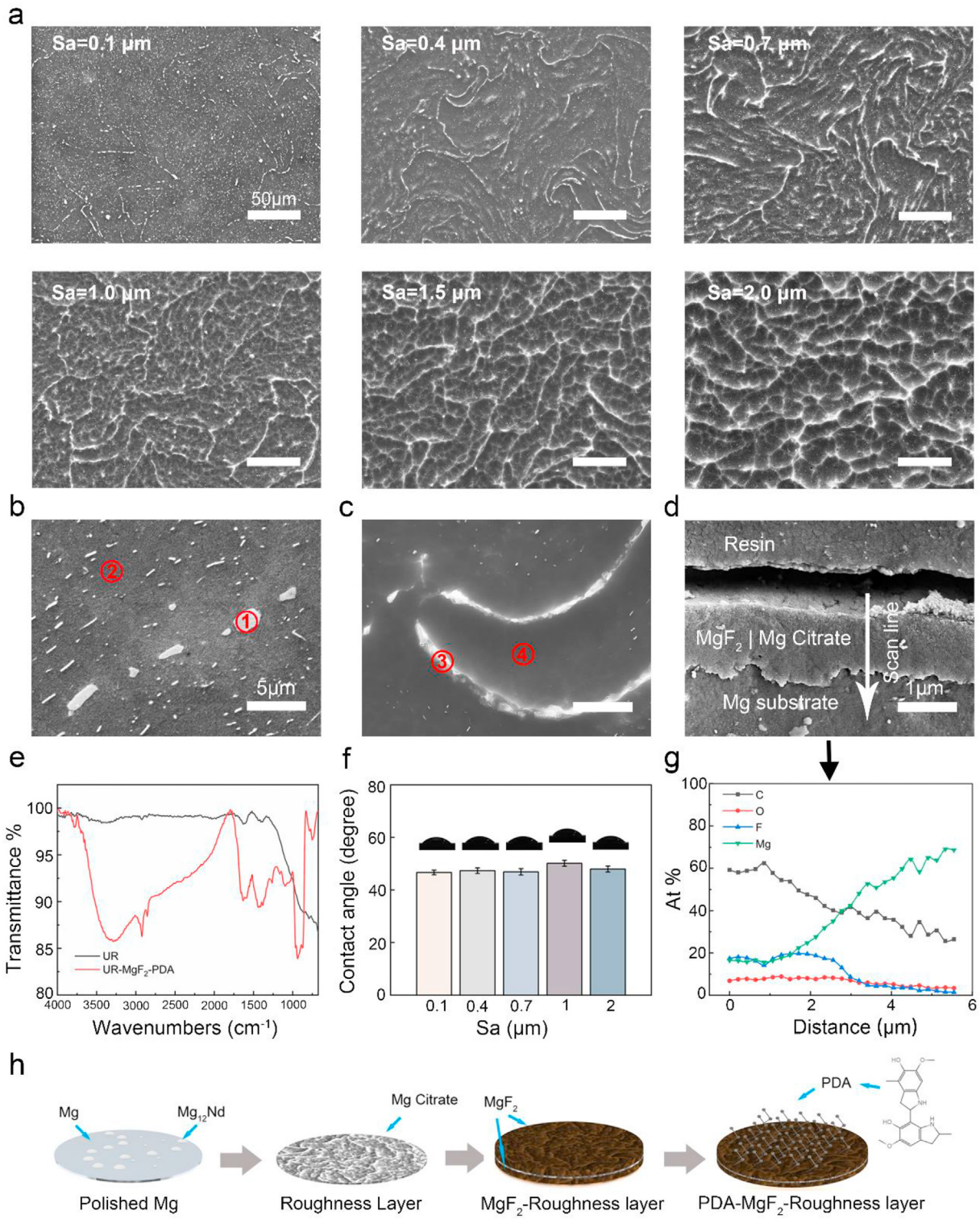

Fig. 3. Surface morphological and chemical characterizations of generated samples. (a) SEM images at different positions along the gradient samples. High-magnification SEM images of samples (b) prior to and (c) post chemical etching. (d) Cross-sectional SEM image and (g) EDS line scan of element profile. (e) ATR-FTIR spectra of Mg samples before and after MgF_2-PDA coating. (f) Static contact angle measurements at different positions along gradients. (h) Schematic illustration of surface alterations after each step of modification.

g revealed the cross-sectional SEM-EDS of samples after fluorination. The variations of F and C implied an MgF_2 conversion layer composited with magnesium citrate, with a thickness of approximately 2 μm. Sample preparation was completed after deposition on top of the MgF_2 of an ultrathin PDA coating in a non-aqueous solution, as reported in our previous work [27]. ATR-FTIR spectra in Fig. 3e demonstrated the existence of polydopamine top coating (3288 cm^{-1}: N–H and O–H; 2924 and 2854 cm^{-1}: aliphatic C–H; 1634 cm^{-1}: C═C; 1095 cm^{-1}: C–O; 937 cm^{-1}: C–H (benzene ring)). Fig. 3f showed similar, moderate wettability of 47–50° water contact angles along the gradients, generally in agreement with the work that reported of a complete PDA coating [28]. It indicated that the surface wetting property was similar

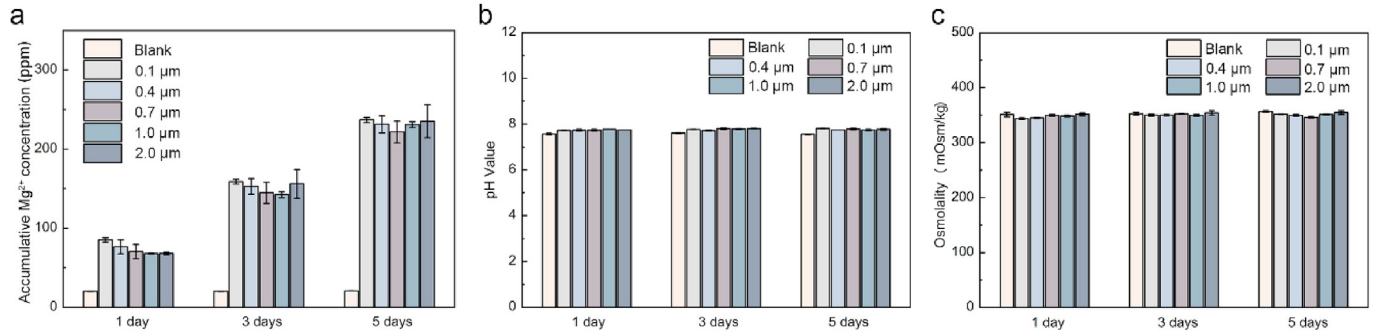

Fig. 4. In vitro short-term degradation results of UR-MgF_2-PDA samples with different surface roughness conducted in DMEM and cell culture conditions. The blank group indicates DMEM culture medium. (a) Accumulative Mg^{2+} concentration, (b) pH value, and (c) osmotic pressure of the sample extracts.

along the gradients. Based on these analyses, the surface chemical and morphological evolution of Mg upon subjected to a series of modifications is schematically illustrated in Fig. 3h.

3.2. Sample degradation & cell viability

The uniform samples with various roughness (Sa = 0.1, 0.4, 0.7, 1.0, and 2.0 μm) were employed to analyze the *in vitro* degradation and cell viability profiles. Sample extracts were collected and evaluated, with results shown in Fig. 4. Notably, as previously proposed for the MgF_2-PDA anti-corrosion coating, the Mg degradation rate decreased significantly compared to the naked Mg. The pH of all groups only slightly elevated to ~7.6 due to a moderate release of OH^-, and the osmotic pressures maintained quite close to that of the physiological medium, around 350 mOsm/kg. The cumulative Mg^{2+} concentrations were generally similar for all the test groups, indicating the surface roughness range under study exerted an inconspicuous effect on the Mg degradation performance.

According to the ISO 10993–5, cytotoxicity of implant materials is required to be no worse than grade I, namely, viability between 75% and 100%. The viability of ECs and SMCs cultured in 50% and 100% concentration of extracts of samples with distinct surface roughness was examined, shown in Fig. S2. The cell viability of all test groups was above 75%. In consideration of the *in vivo* circulation system, it is recommended that extracts can be diluted 6–10 times for cytotoxicity evaluation of degradable metals [29]. All the rough Mg groups basically meet the cytocompatibility requirements. It is also noteworthy that the extracts containing Mg degradation products would slightly inhibit EC viability while barely on SMC.

3.3. Direct cell adhesion and growth on surface roughness gradients

The MgF_2/PDA coating enhanced viability and adhesion of both ECs and SMCs to a very similar extent (Fig. S3). To clarify cellular response to the nano-micrometer roughness on Mg, adhesion and proliferation of ECs and SMCs were assessed by seeding cells directly on the roughness gradients. Fluorescence staining of nuclei and cytoskeleton was displayed in Fig. 5a and statistical results of adherent cell density and projected cell area in Fig. 5b–f.

As shown in Fig. 5b, after 6 h and 1 day, the numbers of attached ECs were similar on the entire gradients without significant difference from the control. After 3 days, however, the ECs density revealed an evident trend along the gradients. It appeared slightly lower than the control for Sa between 0.1 and 0.7 μm, and no statistical difference was observed between the 0.1, 0.4, and 0.7 μm groups. Nevertheless, the cell density remarkably elevated with the increase of roughness at Sa > 0.7 μm. The adherent cell density at Sa = 2.0 μm was double that of Sa = 0.1 μm. Notably, the ECs number at Sa between 1.0 and 2.0 μm significantly exceeded that of the control ($P < 0.05$) by 29.5–43.8%, which formed a nearly confluent monolayer.

With regard to SMCs, it displayed a completely distinct trend in Fig. 5c. While the control group presented a pronounced proliferation profile as expected, cell density on gradients exhibited a general tendency of poor growth for the entire range of Sa between 0.1 and 2.0 μm. After 3 days, SMC density along the gradient samples displayed quite low, with only 36.8%–18.6% of the control.

Moreover, to evaluate the influence of surface roughness on the cell selectivity, the ratio of the density of ECs to SMCs along the gradients was calculated (normalized by that of the control), shown in Fig. 5f. Initially, at 6 h and 1 d, no difference was observed as compared to the control, while on day 3, the cell ratio was greatly enhanced for all the Sa between 0.1 and 2.0 μm, whereas no statistical difference between the 0.1, 0.4, and 0.7 μm groups. Notably, this ratio reached the highest at Sa = 1.0 and 2.0 μm, which was approximately 4.4 times that of the control ($P < 0.001$), implying a significantly enhanced selectivity of ECs over SMCs.

Cell spreading on the roughness gradients presented a different profile from adhesion and growth behaviors. In Fig. 5d and e, the initial spreading area at 6 h and 1 day of both cells on gradients was similar to that of the control. Upon 3-day culture, both cells expanded spreading areas. At Sa between 0.1 and 0.7 μm, ECs and SMCs spreading both tended to gradually reduce as the Sa increased, and remained close for Sa of 0.7–2.0 μm.

3.4. Cell response to Mg kinetic degradation microenvironment

To rule out the influence of continuous release of Mg^{2+} on the cellular response from the above results, ECs and SMCs cultured on plates in Mg kinetic degradation microenvironment was examined for comparison. Transwell inserts were utilized where samples and cells were physically separated by the membranes, meanwhile maintaining Mg^{2+} permeable (Fig. 6a). The instant Mg^{2+} concentration was monitored of 49.9 ± 5.8 ppm (2.08 ± 0.24 mmol/L) after 6 h and 92.4 ± 10.2 ppm (3.85 ± 0.42 mmol/L) on day 1, and after replacement of medium, reached 90.7 ± 2.9 ppm (3.78 ± 0.12 mmol/L) on day 3. There appeared no marked difference between the test group and the control at 6 h and 1d for both cells (Fig. 6b and c). After 3 days, the EC density of the test group was slightly lower than that of the control, specifically, of ~69%. As to SMCs, a negligible difference in cell density was found. Additionally, for both cells, it revealed greater spreading areas upon cultured under Mg degradation than in control, which was more prominent on SMCs. These results demonstrated the controlled release of Mg^{2+} in a range of ≤92.4 ± 10.2 ppm, would induce slight inhibition in ECs proliferation, whereas barely in SMCs growth but cause greater spreading.

3.5. The effects of Mg roughness on cell morphology and subcellular organizations

To reveal more details of cell-substrate interactions,

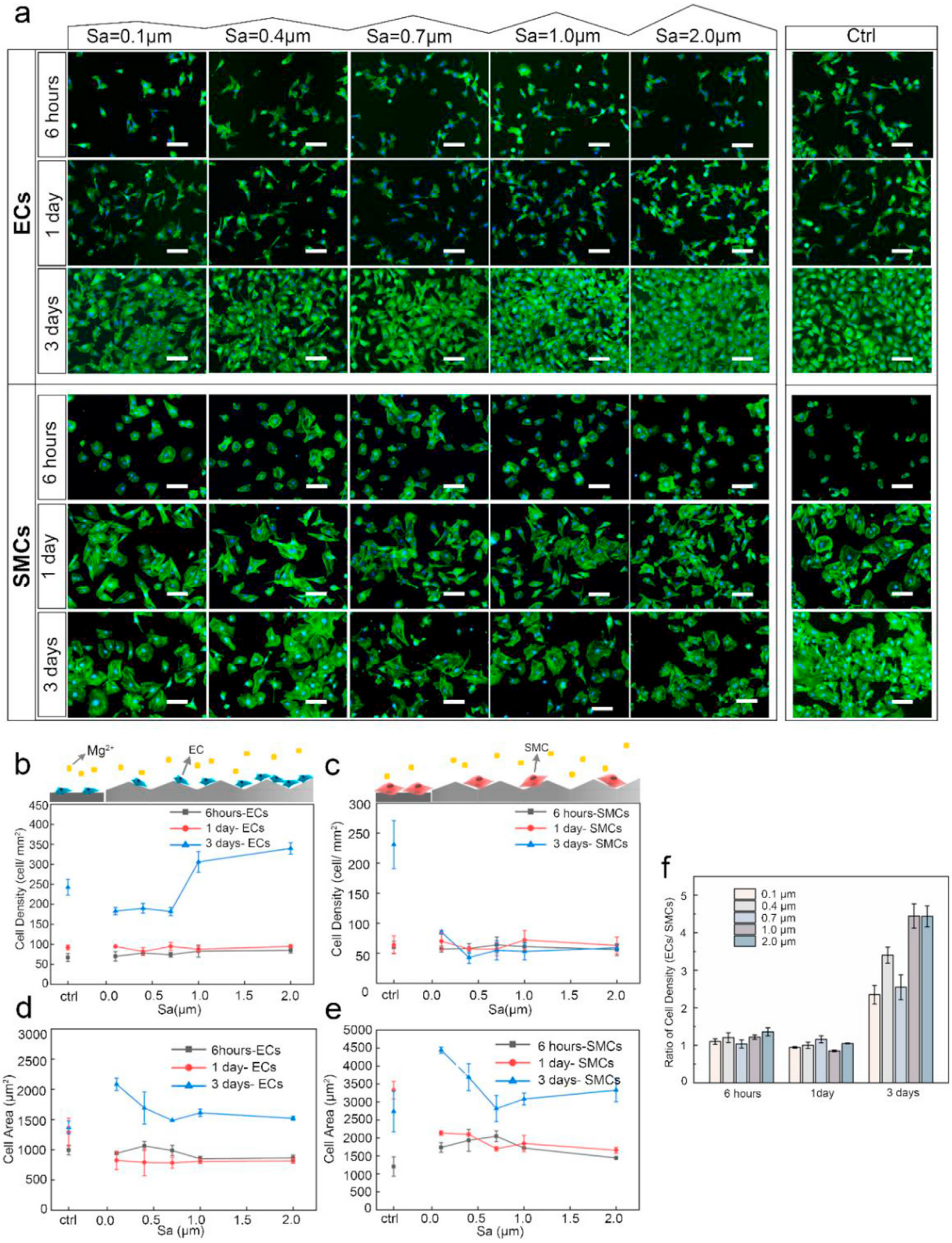

Fig. 5. (a) Direct adhesion of ECs and SMCs on GR-MgF_2-PDA samples observed with fluorescence microscopy for 6 h, 1 day, and 3 days, respectively (scale bar = 100 μm). Statistical results of adherent cell density of EC (b) and SMC (c) and cell spreading area of EC (d) and SMC (e) after cultured for 6 h, 1 day, and 3 days on GR-MgF_2-PDA samples. (f) Calculated ratios of the density of ECs to SMCs at different surface roughness, normalized by the ratio of the blank control group.

immunofluorescence staining and SEM imaging of adherent cells cultured along the gradients were analyzed to provide information on cell spreading morphology, actin cytoskeleton organization, focal adhesion (FA), filopodia formation, and their attachment to the surface features (Fig. 7a and b). Cell adhesion is regulated by dynamic assemblies of structural and signaling proteins that couple the F-actin cytoskeleton to the substrate, where vinculin represents an essential cytoskeletal protein associated with focal adhesion. Generally, large amounts of bright

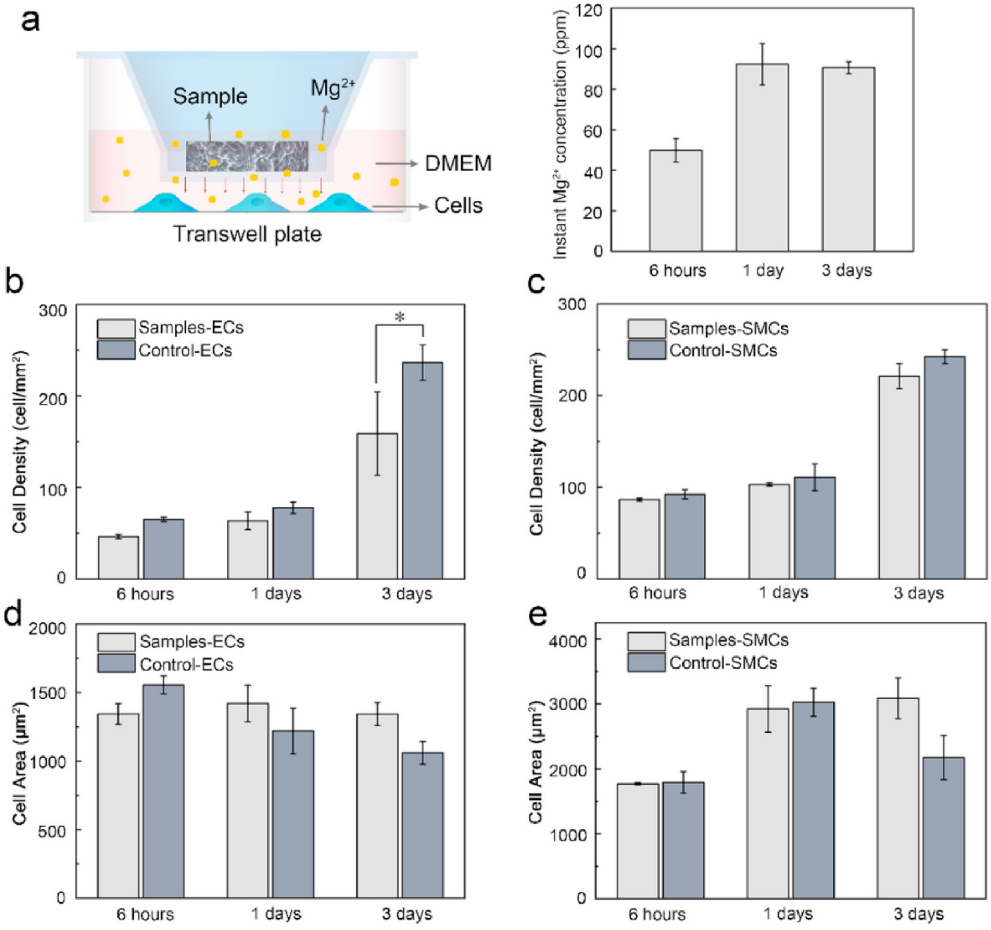

Fig. 6. Cell culture in simulated Mg degradation microenvironment via transwell plate, (a) the experimental device and the real-time Mg^{2+} concentration in the cell culture medium, the cell density of ECs (b) and SMCs (c), the cell spreading area of ECs (d) and SMCs (e). *$P < 0.05$ vs. control.

vinculin signals indicate strong binding strength (mature FA) [30].

For ECs, bright and strong actin expression was observed along the gradients, similar to the control. Nonetheless, unlike the control presenting many mature FAs, the vinculin expression along the gradients appeared less and weaker. Particularly on the flattest part of Sa = 0.1 μm, some cells were observed with only cytosolic vinculin, usually inactive and not recruited to FA. The majority of ECs exhibited normal spreading state, showing similar spread-out morphology as the control. Intriguingly, as the Sa rose above 0.7 μm, a number of more elongated cells appeared. Meanwhile, SEM observation displayed ECs on the rougher part of Sa ≥ 1.0 μm tended to attach exclusively onto the top of the ridges with extended protrusions and filopodia, and bridge over several ridges to suspend over substrates. On the flatter surface of Sa between 0.1 and 0.7 μm, cells appeared more flattened and firmly attached to the surfaces.

As displayed on the control, SMCs along the gradients generally revealed long, thick, and well-organized actin filaments at lower Sa below 0.7 μm. It became slightly disordered upon Sa ≥ 0.7 μm, along with decreased vinculin and FA densities compared with the control. Generally, cell spreading on the gradients became greatly shrunken with diverging morphology. At lower Sa between 0.1 and 0.4 μm, cells exhibited either elongated or compact, polygonal shape. As Sa increased to 0.7–2.0 μm, the majority displayed rhomboid-like morphology of more suppressed spreading. SEM examination further showed SMCs at higher Sa ≥1.0 μm tended to reduce spreading area and adapt to the valley regions for close adhesion onto the substrates. Long pseudopods were observed to extend and attach onto the adjacent valleys, appearing disfavor of direct contact with the raised ridges.

3.6. RT-qPCR analysis of cell gene expressions on Mg rough samples

To further probe the mechanism of cell response to roughness at the gene expression level, we then quantified the expressions of proliferating cell nuclear antigen (PCNA) and vinculin (VCL) for both cell types, and endothelial nitric oxide synthase (eNOs) specifically for ECs [31] (Fig. 7c and d). The expressions of eNOs and PCNA genes for ECs were both remarkably up-regulated at Sa = 2.0 μm by 2.5 and 3.6 folds of the control, respectively ($P < 0.001$), whereas for Sa = 0.1 and 0.7 μm, both were much lower. Meanwhile, VCL expression was down-regulated on all roughness samples. As for SMCs, PCNA gene expression was significantly down-regulated for all roughness groups by more than 50%, consistent with the results of direct adhesion and growth.

4. Discussion

Interfacial cell-material interaction is key to the success of implants. ECs cover the whole inner surface of blood vessels, playing an indispensable role in facilitating endothelialization. In contrast, over proliferation of SMCs is likely to cause hyperplasia, late restenosis, and thrombosis. In view of the adverse events associated with the use of conventional drug-eluting coatings, we sought to explore a distinct approach to regulate vascular cells through engineering surface topography. For the first time, our results demonstrated that ECs and SMCs respond evidently to varying roughness on Mg-based implant material of identical surface chemistry, wettability, and degradation profile. While the MgF_2/PDA anti-corrosion coating improved viability and adhesion of both ECs and SMCs to a similar extent, it is evident that higher surface roughness Sa between 1.0 and 2.0 μm with a network of

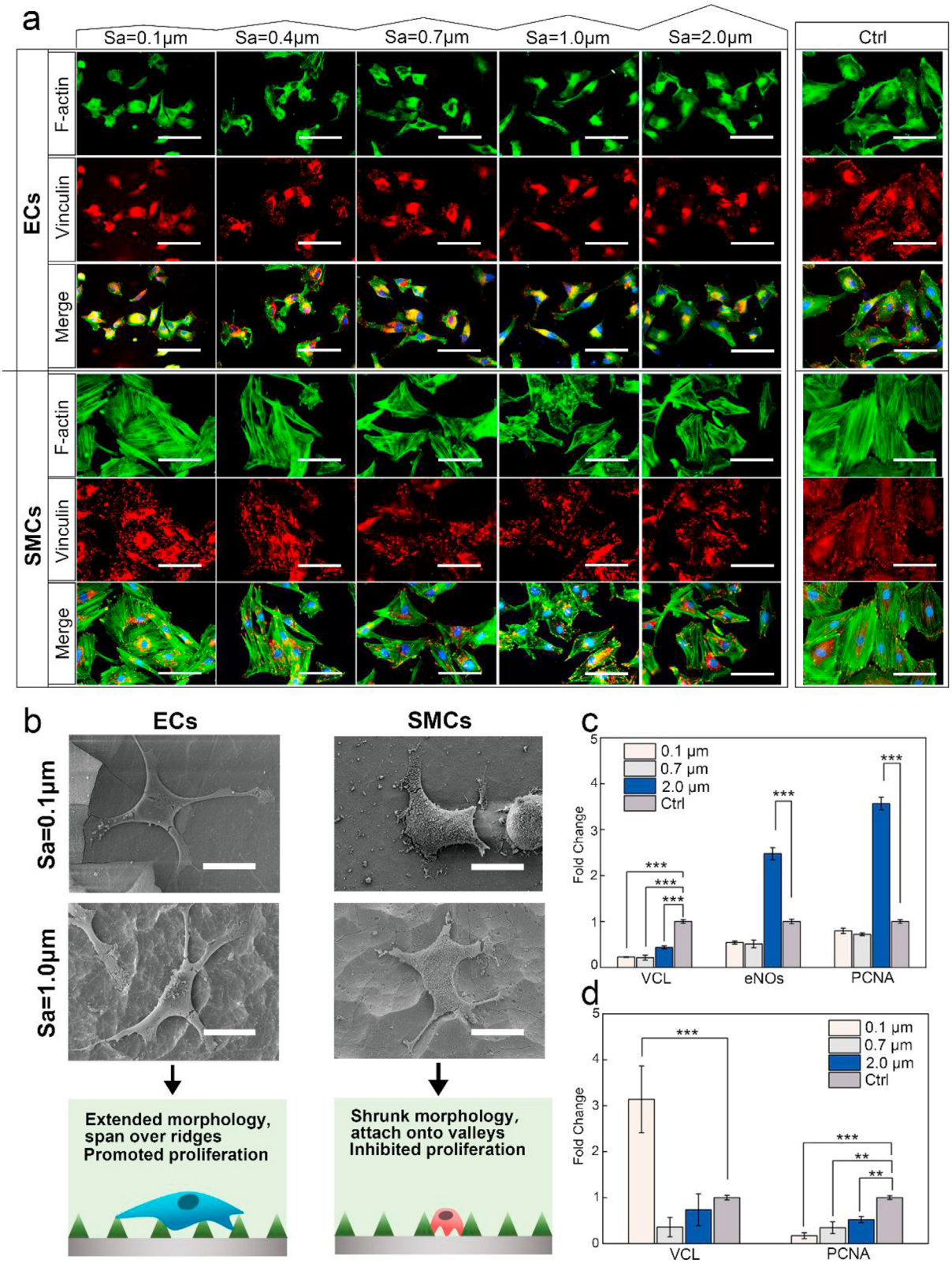

Fig. 7. Immunofluorescence staining (a) and SEM imaging (b) of ECs and SMCs after 1 day culture on the gradients, including F-actin (green), Vinculin (red), and DAPI (blue) staining (scale bar of fluorescence images represented 50 μm, and scale bar of SEM images represented 20 μm). The gene expressions of vinculin (VCL), eNOs and PCNA in ECs (c) and SMCs (d) measured with RT-qPCR (* indicates $P < 0.05$, ** $P < 0.01$, and *** $P < 0.001$). (For interpretation of the references to colour in this figure legend, the reader is referred to the Web version of this article.)

ridge/valley structures provided a most favorable interfacial microenvironment to specifically elicit ECs proliferation while disfavored by SMCs.

Magnesium takes part in various vital cellular reactions to influence viability and functions. It was reported that extracts with Mg^{2+} concentrations of 175 μg/ml (7.2 mM) led to sub-optimal viability of human umbilical vein endothelial cells [32]. Excessive degradation occurs under circumstances of naked Mg or inappropriate surface modifications, causing elevated Mg^{2+}, pH, and osmolality, leading to cell apoptosis. The anti-corrosion MgF_2-PDA coating significantly impeded Mg corrosion, achieving a moderate degradation rate for all the roughness under study, which enhanced cell viability above an acceptable level. Moreover, the PDA top coating could greatly enhance the adhesion and proliferation of both ECs and SMCs to a similar degree (Fig. S3). Nevertheless, there inevitably exists a notable, dynamic elevation of Mg^{2+}, which was monitored of ≤92.4 ppm (3.85 mM) during cell culture. It hardly affected the adhesion and growth of SMCs, but rather slightly suppressing ECs proliferation ($p < 0.05$ vs. control). This result was generally consistent with the previous reports [33]. Apart from (bio)chemical factors, topographical cues play an equally profound role in dictating cellular response. Numerous studies were focused on the linear groove patterns on non-degradable substrates [34]; nonetheless, the impact of other features appeared controversial or unexplored [14]. In our work, in contrast to the insignificant/limited effect of the mild Mg degradation on cells, we found a marked, differential cellular response along the roughness gradients, although the initial cell adhesion displayed similarity. For ECs, at a lower roughness range of Sa between 0.1 and 0.7 μm, cell proliferation remained slightly lower than the control; while the roughness further rose to 1.0–2.0 μm, EC growth was considerably promoted and gradually exceeded that of the control. SMCs response revealed a general significant inhibition trend with slightly higher suppression extent when Sa≥ 0.4 μm.

It should be noteworthy that the observed results actually present the synergistic effects of dynamic Mg degradation and the varying surface morphology. Through comparison with the results obtained in the simply Mg degradation environment, it could be clearly seen that for ECs, at lower roughness of Sa between 0.1 and 0.7 μm, the dynamic release of Mg^{2+}, rather than the surface topography, played a primary role in determining cell response. In contrast, at higher roughness of Sa between 0.7 and 2.0 μm, the significant impact of surface topography overperformed the slight adverse effect of the elevated Mg^{2+}, leading to a pronounced boost of ECs proliferation. Moreover, this stimulation effect appeared gradually intensified with increasing surface roughness, which reached the maximum at the highest Sa = 2.0 μm, significantly exceeding the control. This finding is generally consistent with some previous reports on submicro-microscale rough samples, although with different patterns and substrates [11,35]. As for SMCs, the entire range of nano-micrometer roughness of Sa between 0.1 and 2.0 μm, instead of the released Mg^{2+}, induced suppression effect on cell growth.

Mechanical cue (topography, stiffness, etc.) is extensively reported to have a substantial role in determining the fate of cells, where specific signaling pathways (e.g., MAPK [36]) control the transduction of extracellular stimuli into a series of intracellular biochemical reactions. We also found altered cell spreading, attachment mode, and focal adhesion with varying surface topography dimensions. ECs and SMCs formed interaction with the surface patterns in strikingly different manners, particularly at a higher roughness range of Sa between 0.7 and 2.0 μm. While ECs spanned over several ridges through long, thick protrusions and filopodia, SMCs appeared forced to decrease the spreading morphology to adapt onto the valleys. Intriguingly, similar phenomena were observed on aligned groove arrays for ECs adhesion and spreading, but different from those on pillar patterns [14]. On the other hand, SMCs revealed exquisitely sensitive to surface morphology stimuli, as consistently reported with shrunk morphology on nanostructured surface of Ra between ~20 and 300 nm [34], and micron-scale patterns of grooves and pillars [14]. It is most probable that the cell body does not directly interact with this topography cue, instead, through a sensing mechanism performed by fundamental subcellular structures of filopodia and focal adhesions, which not only act as biochemical signal transducers but also mechanical sensors [37]. Consequently, signal transduction for adaptive changes in gene expression profile was generated to regulate cell behaviors and functions, as manifested by the significant alterations in PCNA and VCL genes for both ECs and SMCs in response to different roughness. Furthermore, significant elevation of eNOs expression of ECs at higher roughness suggested a potential increase of NO production, which would contribute to EC growth [38], vasomotor function, and restrict thrombosis and SMCs hyperplasia as well [39].

5. Conclusions

In summary, our work presented a facile, reproducible method for fabricating surface roughness gradients with nano-micrometer roughness variation on a biodegradable Mg. In a second step, the generated gradients facilitated a comprehensive, high-throughput investigation of the response of vascular cells to surface topography cues under controlled Mg degradation. With confirmed homogeneous surface chemistry and wettability, the cellular assays on the obtained gradients disclosed dramatically distinct behaviors of ECs and SMCs regarding adhesion, spreading, and growth in a roughness-dependent manner. The increase of roughness from nanoscale to submicro-microscale could remarkably promote ECs proliferation and function under a slightly adverse influence of Mg degradation. The entire nano-micrometer roughness range greatly suppressed SMCs growth and spreading on Mg, which was more conspicuous on submicro-micro texture. We were also able to gain further insights into the underlying modulatory mechanism, presumably involving mechanical sensing and transduction mediated with focal adhesion and filopodia to regulate related gene expressions. In addition, an optimized micro-roughness range of Sa between 1.0 and 2.0 μm with ridge/valley network texture was identified to most significantly enhance the selectivity of ECs over SMCs. Thus, it may be of direct implications in bioresorbable vascular implants, in particular, tailoring surface topography design to improve endothelialization and enhance bioefficacy.

CRediT authorship contribution statement

Ke Zhou: Conceptualization, Methodology, Validation, Formal analysis, Investigation, Resources, Writing - original draft, Writing - review & editing. **Yutong Li:** Conceptualization, Methodology, Investigation. **Lei Zhang:** Resources. **Liang Jin:** Investigation. **Feng Yuan:** Investigation. **Jinyun Tan:** Supervision. **Guangyin Yuan:** Supervision, Project administration, Funding acquisition. **Jia Pei:** Supervision, Project administration, Funding acquisition.

Declaration of competing interest

The authors declare that they have no known competing financial interests or personal relationships that could have appeared to influence the work reported in this paper.

Acknowledgements

This work was supported by the National Key Research and Development Program of China [grant numbers 2016YFC1102401, 2016YFB0301001]; National Natural Science Foundation of China [grant number 51701041]; the Committee of Shanghai Science and Technology [grant number 17DZ2200200] and Shanghai Outstanding Academic Leaders Plan [grant number 17XD1402100]. Ke Zhou and Yutong Li contributed equally to this work.

Appendix A. Supplementary data

Supplementary data to this article can be found online at https://doi.org/10.1016/j.bioactmat.2020.08.004.

References

[1] E.J. Benjamin, S.S. Virani, C.W. Callaway, A.M. Chamberlain, A.R. Chang, S. Cheng, S.E. Chiuve, M. Cushman, F.N. Delling, R. Deo, S.D. de Ferranti, J.F. Ferguson, M. Fornage, C. Gillespie, C.R. Isasi, M.C. Jimenez, L.C. Jordan, S.E. Judd, D. Lackland, J.H. Lichtman, L. Lisabeth, S. Liu, C.T. Longenecker, P.L. Lutsey, J.S. Mackey, D.B. Matchar, K. Matsushita, M.E. Mussolino, K. Nasir, M. O'Flaherty, L.P. Palaniappan, A. Pandey, D.K. Pandey, M.J. Reeves, M.D. Ritchey, C.J. Rodriguez, G.A. Roth, W.D. Rosamond, U.K.A. Sampson, G.M. Satou, S.H. Shah, N.L. Spartano, D.L. Tirschwell, C.W. Tsao, J.H. Voeks, J.Z. Willey, J.T. Wilkins, J.H. Wu, H.M. Alger, S.S. Wong, P. Muntner, E. American Heart Association Council on, C. Prevention Statistics, S. Stroke Statistics, Heart disease and stroke statistics-2018 update: a report from the American heart association, Circulation 137 (2018) 67–492.

[2] A. Gruntzig, U. Kuhlmann, W. Vetter, U. Lutolf, B. Meier, W. Siegenthaler, Treatment of renovascular hypertension with percutaneous transluminal dilatation of a renal-artery stenosis, Lancet (London, England) 1 (1978) 801–802.

[3] P.K. Bowen, E.R. Shearier, S. Zhao, R.J. Guillory, II, F. Zhao, J. Goldman, J.W. Drelich, Biodegradable metals for cardiovascular stents: from clinical concerns to recent Zn-alloys, Adv. Healthc. Mater. 5 (2016) 1121–1140.

[4] N.A. Scott, Restenosis following implantation of bare metal coronary stents: pathophysiology and pathways involved in the vascular response to injury, Adv. Drug Deliv. Rev. 58 (2006) 358–376.

[5] D. Hoare, A. Bussooa, S. Neale, N. Mirzai, J. Mercer, The future of cardiovascular stents: bioresorbable and integrated biosensor Technology, Adv. Sci. 6 (2019).

[6] S. Chen, Z. Yao, Y. Guan, H. Yang, M.B. Shahzad, Y. Wu, B. Zhang, L. Shen, K. Yang, High nitrogen stainless steel drug-eluting stent - assessment of pharmacokinetics and preclinical safety in vivo, Bioactive. Mater 5 (2020) 779–786.

[7] H. Kerdjoudj, C. Boura, V. Moby, K. Montagne, P. Schaaf, J.C. Voegel, J.F. Stoltz, P. Menu, Re-endothelialization of human umbilical arteries treated with polyelectrolyte multilayers: a tool for damaged vessel replacement, Adv. Funct. Mater. 17 (2007) 2667–2673.

[8] D.J. Kereiakes, I.T. Meredith, S. Windecker, R.L. Jobe, S.R. Mehta, I.J. Sarembock, R.L. Feldman, B. Stein, C. Dubois, T. Grady, S. Saito, T. Kimura, T. Christen, D.J. Allocco, K.D. Dawkins, Efficacy and safety of a novel bioabsorbable polymer-coated, everolimus-eluting coronary stent the EVOLVE II randomized trial, Circ.-Cardiovasc. Interv. 8 (2015).

[9] S. Werner, R. Grose, Regulation of wound healing by growth factors and cytokines, Physiol. Rev. 83 (2003) 835–870.

[10] W. Jiang, D. Rutherford, T. Vuong, H. Liu, Nanomaterials for treating cardiovascular diseases: a review, Bioactiv. Mater. 2 (2017) 185–198.

[11] M.F.A. Cutiongco, S.H. Goh, R. Aid-Launais, C. Le Visage, H.Y. Low, E.K.F. Yim, Planar and tubular patterning of micro and nano-topographies on poly(vinyl alcohol) hydrogel for improved endothelial cell responses, Biomaterials 84 (2016) 184–195.

[12] R. Schieber, F. Lasserre, M. Hans, M. Fernandez-Yaguee, M. Diaz-Ricart, G. Escolar, M.-P. Ginebra, F. Muecklich, M. Pegueroles, Direct laser interference patterning of CoCr alloy surfaces to control endothelial cell and platelet response for cardiovascular applications, Adv. Healthc. Mater. 6 (2017).

[13] L.-H. Cui, H.J. Joo, D.H. Kim, H.-R. Seo, J.S. Kim, S.-C. Choi, L.-H. Huang, J.E. Na, I.R. Lim, J.-H. Kim, I.J. Rhyu, S.J. Hong, K.B. Lee, D.-S. Lim, Manipulation of the response of human endothelial colony-forming cells by focal adhesion assembly using gradient nanopattern plates, Acta Biomater. 65 (2018) 272–282.

[14] Y. Ding, Z. Yang, C.W.C. Bi, M. Yang, S.L. Xu, X. Lu, N. Huang, P. Huang, Y. Leng, Directing vascular cell selectivity and hemocompatibility on patterned platforms featuring variable topographic geometry and size, ACS Appl. Mater. Interfaces 6 (2014) 12062–12070.

[15] C. Aktas, E. Doerrschuck, C. Schuh, M.M. Miro, J. Lee, N. Puetz, G. Wennemuth, W. Metzger, M. Oberringer, M. Veith, H. Abdul-Khaliq, Micro- and nanostructured Al2O3 surfaces for controlled vascular endothelial and smooth muscle cell adhesion and proliferation, Mater. Sci. Eng. C-Mater. Biol. Appl. 32 (2012) 1017–1024.

[16] C. Liang, Y. Hu, H. Wang, D. Xia, Q. Li, J. Zhang, J. Yang, B. Li, H. Li, D. Han, M. Dong, Biomimetic cardiovascular stents for in vivo re-endothelialization, Biomater. 103 (2016) 170–182.

[17] S. Morgenthaler, C. Zink, N.D. Spencer, Surface-chemical and -morphological gradients, Soft Matter 4 (2008) 419.

[18] R.R. Bhat, B.N. Chaney, J. Rowley, A. Liebmann-Vinson, J. Genzer, Tailoring cell adhesion using surface-grafted polymer gradient assemblies, Adv. Mater. 17 (2005) 2802–2807.

[19] Y. Hou, W. Xie, L. Yu, L.C. Camacho, C. Nie, M. Zhang, R. Haag, Q. Wei, Surface roughness gradients reveal topography-specific mechanosensitive responses in human mesenchymal stem cells, Small 16 (2020) e1905422.

[20] R. Zeng, W. Dietzel, F. Witte, N. Hort, C. Blawert, Progress and challenge for magnesium alloys as biomaterials, Adv. Eng. Mater. 10 (2008) B3–B14.

[21] J. Fu, Y. Su, Y.X. Qin, Y. Zheng, Y. Wang, D. Zhu, Evolution of metallic cardiovascular stent materials: a comparative study among stainless steel, magnesium and zinc, Biomaterials 230 (2020) 119641.

[22] D.H. Zhu, J. You, N. Zhao, H.X. Xu, Magnesium regulates endothelial barrier functions through TRPM7, MagT1, and S1P1, Adv. Sci. 6 (2019) 13.

[23] L. Mao, L. Shen, J. Niu, J. Zhang, W. Ding, Y. Wu, R. Fan, G. Yuan, Nanophasic biodegradation enhances the durability and biocompatibility of magnesium alloys for the next-generation vascular stents, Nanoscale 5 (2013) 9517–9522.

[24] X. Zheng, J. Dong, Y. Xiang, J. Chang, F. Wang, L. Jin, Y. Wang, W. Ding, Formability, mechanical and corrosive properties of Mg–Nd–Zn–Zr magnesium alloy seamless tubes, Mater. Des. 31 (2010) 1417–1422.

[25] L. Mao, L. Shen, J. Chen, Y. Wu, M. Kwak, Y. Lu, Q. Xue, J. Pei, L. Zhang, G. Yuan, R. Fan, J. Ge, W. Ding, Enhanced bioactivity of Mg-Nd-Zn-Zr alloy achieved with nanoscale MgF2 surface for vascular stent application, ACS Appl. Mater. Interfaces 7 (2015) 5320–5330.

[26] L. Mao, G. Yuan, S. Wang, J. Niu, G. Wu, W. Ding, A novel biodegradable Mg-Nd-Zn-Zr alloy with uniform corrosion behavior in artificial plasma, Mater. Lett. 88 (2012) 1–4.

[27] F. Yuan, A Novel Multifunctional Nanoscale Coating Based on Biomimetic Surface Engineering for Magnesium Alloy-Based Stents Application, Shanghai Jiao Tong University, 2018.

[28] Y. Jiang, K. Shi, H. Tang, Y. Wang, Enhanced wettability and wear resistance on TiO2/PDA thin films prepared by sol-gel dip coating, Surf. Coating. Technol. 375 (2019) 334–340.

[29] J. Wang, F. Witte, T. Xi, Y. Zheng, K. Yang, Y. Yang, D. Zhao, J. Meng, Y. Li, W. Li, K. Chan, L. Qin, Recommendation for modifying current cytotoxicity testing standards for biodegradable magnesium-based materials, Acta Biomater. 21 (2015) 237–249.

[30] S. Tojkander, G. Gateva, P. Lappalainen, Actin stress fibers - assembly, dynamics and biological roles, J. Cell Sci. 125 (2012) 1855–1864.

[31] F. Gao, Y. Hu, G. Li, S. Liu, L. Quan, Z. Yang, Y. Wei, C. Pan, Layer-by-layer deposition of bioactive layers on magnesium alloy stent materials to improve corrosion resistance and biocompatibility, Bioactive materials 5 (2020) 611–623.

[32] X. Gu, Y. Zheng, Y. Cheng, S. Zhong, T. Xi, In vitro corrosion and biocompatibility of binary magnesium alloys, Biomaterials 30 (2009) 484–498.

[33] J. Ma, N. Zhao, D. Zhu, Biphasic responses of human vascular smooth muscle cells to magnesium ion, J. Biomed. Mater. Res. 104 (2016) 347–356.

[34] S.A. Biela, Y. Su, J.P. Spatz, R. Kemkemer, Different sensitivity of human endothelial cells, smooth muscle cells and fibroblasts to topography in the nano-micro range, Acta Biomater. 5 (2009) 2460–2466.

[35] Y. Shen, G. Wang, L. Chen, H. Li, P. Yu, M. Bai, Q. Zhang, J. Lee, Q. Yu, Investigation of surface endothelialization on biomedical nitinol (NiTi) alloy: effects of surface micropatterning combined with plasma nanocoatings, Acta Biomater. 5 (2009) 3593–3604.

[36] C.Q. Yi, D.D. Liu, C.C. Fong, J.C. Zhang, M.S. Yang, Gold nanoparticles promote osteogenic differentiation of mesenchymal stem cells through p38 MAPK pathway, ACS Nano 4 (2010) 6439–6448.

[37] C.H. Seo, K. Furukawa, K. Montagne, H. Jeong, T. Ushida, The effect of substrate microtopography on focal adhesion maturation and actin organization via the RhoA/ROCK pathway, Biomaterials 32 (2011) 9568–9575.

[38] H. Qiu, P. Qi, J. Liu, Y. Yang, X. Tan, Y. Xiao, M.F. Maitz, N. Huang, Z. Yang, Biomimetic engineering endothelium-like coating on cardiovascular stent through heparin and nitric oxide-generating compound synergistic modification strategy, Biomaterials 207 (2019) 10–22.

[39] H. Cai, D.G. Harrison, Endothelial dysfunction in cardiovascular diseases - the role of oxidant stress, Circ. Res. 87 (2000) 840–844.